Front. Mater. Sci. 2023, 17(3): 230651
https://doi.org/10.1007/s11706-023-0651-y

RESEARCH ARTICLE

Amorphous Sn modified nitrogen-doped porous carbon nanosheets with rapid capacitive mechanism for high-capacity and fast-charging lithium-ion batteries

Chong Xu*, Guang Ma*, Wang Yang (✉), Sai Che, Neng Chen, Ni Wu, Bo Jiang, Ye Wang, Yankun Sun, Sijia Liao, Jiahao Yang, Xiang Li, Guoyong Huang, and Yongfeng Li (✉)

State Key Laboratory of Heavy Oil Processing, China University of Petroleum, Beijing 102249, China

ABSTRACT: Sn-based materials are considered as a kind of potential anode materials for lithium-ion batteries (LIBs) owing to their high theoretical capacity. However, their use is limited by large volume expansion deriving from the lithiation/delithiation process. In this work, amorphous Sn modified nitrogen-doped porous carbon nanosheets (ASn-NPCNs) are obtained. The synergistic effect of amorphous Sn and high edge-nitrogen-doped level porous carbon nanosheets provides ASn-NPCNs with multiple advantages containing abundant defect sites, high specific surface area (214.9 $m^2 \cdot g^{-1}$), and rich hierarchical pores, which can promote the lithium-ion storage. Serving as the LIB anode, the as-prepared ASn-NPCNs-750 electrode exhibits an ultrahigh capacity of 1643 $mAh \cdot g^{-1}$ at 0.1 $A \cdot g^{-1}$, ultrafast rate performance of 490 $mAh \cdot g^{-1}$ at 10 $A \cdot g^{-1}$, and superior long-term cycling performance of 988 $mAh \cdot g^{-1}$ at 1 $A \cdot g^{-1}$ after 2000 cycles with a capacity retention of 98.9%. Furthermore, the in-depth electrochemical kinetic test confirms that the ultrahigh-capacity and fast-charging performance of the ASn-NPCNs-750 electrode is ascribed to the rapid capacitive mechanism. These impressive results indicate that ASn-NPCNs-750 can be a potential anode material for high-capacity and fast-charging LIBs.

KEYWORDS: amorphous Sn; rapid capacitive mechanism; lithium-ion storage; nitrogen-doped carbon; fast charging

Contents

1 Introduction

With the continuous progress of society and the vigorous

Received February 21, 2023; accepted May 10, 2023

E-mails: yfli@cup.edu.cn (Y.L.), wyang@cup.edu.cn (W.Y.)

* C.X. and G.M. contributed equally to this work and should be considered as co-first authors.

development of science and technology, requirements for the endurance of new energy vehicles and portable devices are gradually improved [1–7]. Rechargeable lithium-ion batteries (LIBs), as a kind of secondary batteries, are widely used owing to their ultrahigh energy density and long service life [8–11]. Nevertheless, the graphite anode is difficult to satisfy the requirement of high-performance LIBs due to the low theoretical specific capacity (372 $\mathrm{mAh \cdot g^{-1}}$) [12–15]. Hence, it is necessary to investigate substitute anode materials with high capacity, ultrafast rate performance and excellent cycle stability to satisfy the requirements of high-performance LIBs. Metallic Sn anode materials are widely investigated owing to their excellent conductivity and high theoretical capacity (994 $\mathrm{mAh \cdot g^{-1}}$) [16–19]. Unfortunately, Sn anode materials illustrate unacceptable capacity fading during cycling due to the pulverization resulting from large volume expansion, which is caused by the repeated lithium-ion insertion/extraction [20–22].

In order to overcome difficulties in the application of Sn anode materials, many significant research schemes have been proposed. One scheme is to combine active and inactive metal components, developing a firm structure of metal–Sn alloy (Ni–Sn alloy, Co–Sn alloy, etc.) [23–25], and the other scheme is to construct nanostructured Sn-based materials with shortened lithium-diffusion length and reduced internal strain, such as Sn-based nanowires, nanospheres, and nanotubes [26–28]. Besides, compared with crystalline Sn materials, the short-range sequence of amorphous Sn anode materials can provide more abundant lithium intercalation sites and effectively release structural strain in the repeated lithium-ion insertion/extraction process, thus improving the structural integrity of the Sn-based electrode [29]. Furthermore, much more schemes have been concentrated on combining carbonaceous materials to fabricate Sn/C composites. Carbonaceous buffer matrices, such as carbon dots, carbon nanofibers, carbon nanotubes, graphene, and porous carbon materials, have been widely investigated and demonstrated with improved electrochemical performance [30–34]. These carbonaceous materials can successfully buffer the strain resulting from the volume expansion of Sn and stabilize the structure of the electrode, incurring greatly enhanced rate performance and cycling stability. Furthermore, the nitrogen doping has been demonstrated as an efficient strategy for carbonaceous materials to enhance the lithium-ion storage by introducing the supplementary surface induced lithium-ion adsorption mechanism and promoting the electrical conductivity of materials [35]. As a two-dimensional (2D) material and superior nitrogen source, g-C_3N_4 is widely used in the preparation of LIBs anode materials because of its high nitrogen content, low cost, and simple preparation methods [36–42]. Generally, g-C_3N_4 as a template can not only avoid the metal particles aggregation during the preparation process, but also self-decompose to facilitate the construction of porous structure at high temperatures, providing abundant lithium-ion storage sites [43–46]. Even these strategies are carried out, there are challenges such as high cost, strong precursor toxicity, and complicated preparation processes to synthesize high-performance Sn/C anode materials for LIBs via the combination of amorphous Sn and nitrogen-doped porous carbon materials [4,6,13].

Therefore, we have synthesized amorphous Sn modified nitrogen-doped porous carbon nanosheets (ASn-NPCNs) through hydrothermal and annealing strategy to overcome these challenges. The decomposition of g-C_3N_4 and successful doping of nitrogen provide a rich pore structure and high specific surface area for ASn-NPCNs, which is conducive to the lithium-ion storage and the rapid transmission of electrons. ASn-NPCNs display unique 2D porous nanosheet structure and ultrahigh nitrogen doping level (> 15.18 at.%). When used as the LIB anode, the ASn-NPCNs-750 electrode delivers high capacity (1643 $\mathrm{mAh \cdot g^{-1}}$ at 0.1 $\mathrm{A \cdot g^{-1}}$), ultrafast rate performance (490 $\mathrm{mAh \cdot g^{-1}}$ at 10 $\mathrm{A \cdot g^{-1}}$), and superior long-term cycling performance (988 $\mathrm{mAh \cdot g^{-1}}$ at 1 $\mathrm{A \cdot g^{-1}}$ after 2000 cycles with a capacity retention of 98.9%). Moreover, amorphous Sn can not only provide high capacity, but also reduce electrode pulverization to ensure the structural integrity of the electrode, thus extending the cycle life.

2 Experimental

2.1 Sample preparation

The g-C_3N_4 was obtained by thermal polycondensation of melamine in a muffle furnace under 550 °C for 4 h. Typically 20 g of melamine was added into a crucible with a lid, which was then transferred to a muffle furnace. The melamine was heated to 550 °C with a ramp rate of 2.5 $\mathrm{°C \cdot min^{-1}}$ and kept at 550 °C for 4 h. After cooling down naturally to room temperature, the resultant yellow bulk product was ground into powder using a Soybean

Milk machine, obtaining the g-C_3N_4.

ASn-NPCNs-*T* (*T* = 650, 750, and 850) samples were synthesized via a simple hydrothermal and pyrolysis strategy. Taking ASn-NPCNs-750 for example, 1 g $SnCl_4$, 2 g g-C_3N_4, and 6 g glucose were added into 60 mL water with stirring for 2 h to make it dispersed uniformly. Then, the mixed solution was transferred into a 100 mL Teflon-lined stainless-steel autoclave and treated at 180 °C for 4 h. Subsequently, the obtained precursor was centrifuged and washed with distilled water and then dried in vacuum oven at 80 °C for 12 h. Finally, the obtained precursor was annealed at 750 °C for 1 h with a ramping rate of 5 $°C\cdot min^{-1}$ under Ar atmosphere to obtain ASn-NPCNs-750.

The ASn-PC-750 (amorphous Sn modified porous carbon nanosheets) was prepared under the same conditions as ASn-NPCNs-750, except that no g-C_3N_4 was added.

The NPCNs-750 (nitrogen-doped porous carbon nanosheets) was prepared under the same conditions as ASn-NPCNs-750, except that no $SnCl_4$ was added.

2.2 Material characterization

The morphologies of the as-prepared samples were characterized by scanning electron microscopy (SEM; SU8010) and transmission electron microscopy (TEM; JEOL JSM-2100). The structure features and crystal phases of as-prepared samples were explored by powder X-ray diffraction (XRD; Miniflex, Rigaku) and Raman spectroscopy (Horiba, 532 nm laser excitation). The specific surface area and the pore size distribution were investigated via a nitrogen gas sorption surface area tester (JW-BK132F). The elemental compositions of as-prepared samples were confirmed by X-ray photoelectron spectroscopy (XPS; K-Alpha 1063 spectrometer).

2.3 Electrochemical measurements

The Li^+ storage performances of the as-prepared samples were evaluated by assembling CR2032 coin half-cells. The slurry was prepared by mixing active materials (80%), Super P (10%), and polyvinylidene fluoride (PVDF; 10%), and then coated on a Cu foil and dried at 100 °C for 10 h to obtain the working electrode. The mass loading of active materials in the working electrode was about 1.3–1.6 $mg\cdot cm^{-2}$. The electrolyte was 1.0 $mol\cdot L^{-1}$ $LiPF_6$ mixed in a solvent of dimethyl carbonate (DMC) and ethylene carbonate (EC) with a volume ratio of 1:1. Lithium foil was used as the counter electrode. The galvanostatic charge/discharge cycling was tested on a battery test system (LAND CT2001A) at 25 °C with a voltage range of 0.01–3 V. The cyclic voltammetry (CV) was performed by the CHI 760E. The electrochemical impedance spectroscopy (EIS) was applied by the CS350/CS16X workstation.

3 Results and discussion

The procedure for the synthesis of ASn-NPCNs-*T* composites is shown in Fig. 1. In the typical synthesis process, $SnCl_4$ is used as the Sn source, while glucose and g-C_3N_4 are utilized as carbon and nitrogen sources. Glucose carbide and Sn derivatives are uniformly coated on the surface of the g-C_3N_4 template during the hydrothermal treatment step. Then g-C_3N_4 starts to decompose as a self-decomposition template in the subsequent annealing process (*t* = 650, 750, or 850 °C), and gradually forms a nitrogen-doped porous carbon nanosheets structure with rich hierarchical pores. Notably, the self-decomposition effect of the g-C_3N_4 template promotes the formation of the 2D porous carbon nanosheet structure.

The microstructure and the morphology of ASn-NPCNs-*T* samples were probed by SEM and TEM. Figures 2(a)–2(f) indicate that ASn-NPCNs-650 and ASn-NPCNs-750 evidently have a crimped lamellar structure

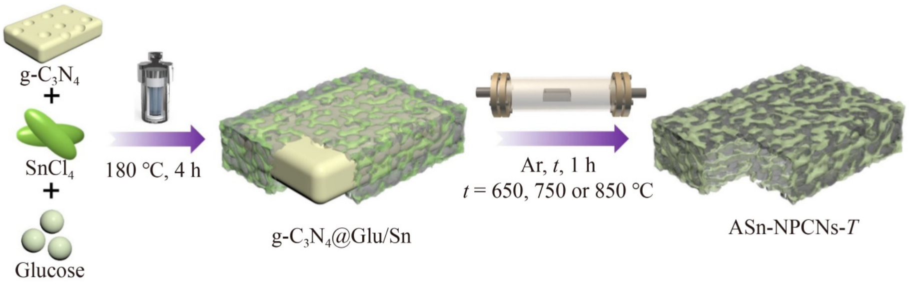

Fig. 1 Schematic illustration of the synthesis of ASn-NPCNs-*T*.

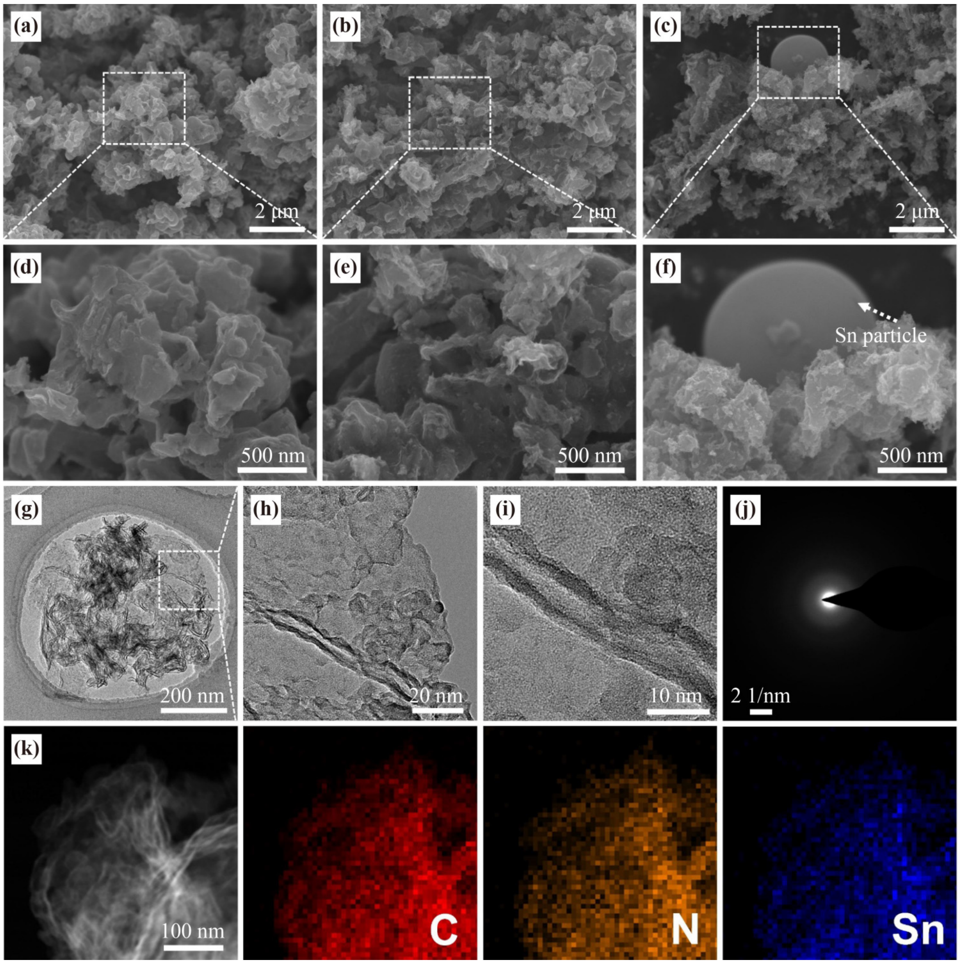

Fig. 2 Morphology characterizations: SEM images of (**a**)(**d**) ASn-NPCNs-650, (**b**)(**e**) ASn-NPCNs-750, and (**c**)(**f**) ASn-NPCNs-850; (**g**)(**h**) TEM images and (**i**) HRTEM image of ASn-NPCNs-750; (**j**) SAED pattern of ASn-NPCNs-750; (**k**) EDX mapping images of ASn-NPCNs-750.

with a certain degree of aggregation. However, an obvious Sn particle appeared in ASn-NPCNs-850, which may be due to the high annealing temperature leading to the transformation of amorphous Sn into crystalline Sn. Interestingly, without g-C_3N_4 as a template, the sample (ASn-PC-750) will form heavily aggregated porous carbon (Figs. S1(a) and S1(c)). In addition, when no $SnCl_4$ is added, the carbon layer of NPCNs-750 is thinner and more transparent (Figs. S1(b) and S1(d)). The microscopic structure and the internal morphology of such samples are further explored by TEM and HRTEM. It can be seen from Figs. 2(g)–2(i) that ASn-NPCNs-750 shows a 2D sheet structure which is similar to the morphology of the g-C_3N_4 template. Moreover, the selected area electron diffraction (SAED) pattern of ASn-NPCNs-750 shows no obvious diffraction rings, indicating the typical amorphous structure (Fig. 2(j)) [47]. In addition, the elemental mapping analysis of ASn-NPCNs-750 demonstrates the homogenous distribution of C, N, and Sn elements (Fig. 2(k)).

The chemical compositions of ASn-NPCNs-*T* samples were investigated by XRD and thermogravimetric analysis (TGA) under air atmosphere. As illustrated in Fig. 3(a), ASn-NPCNs-650 and ASn-NPCNs-750 have no obvious strong peaks, which prove that Sn exists in an amorphous phase in these samples and there is no residual g-C_3N_4 (Fig. S2). However, the diffraction peaks of ASn-NPCNs-850 are ascribed to the characteristic peaks of Sn (JCPDS card no. 04-0673), which proves the existence of crystalline Sn. This result is consistent with those from SEM and TEM. Therefore, the increase of the annealing temperature will promote the transformation of amorphous Sn into crystalline Sn. Neither ASn-PC-750 nor NPCNs-750 shows a characteristic peak related to crystalline Sn (Fig. S3). As revealed in Fig. 3(b), a little decrease of weight below 200 °C is ascribed to the loss of

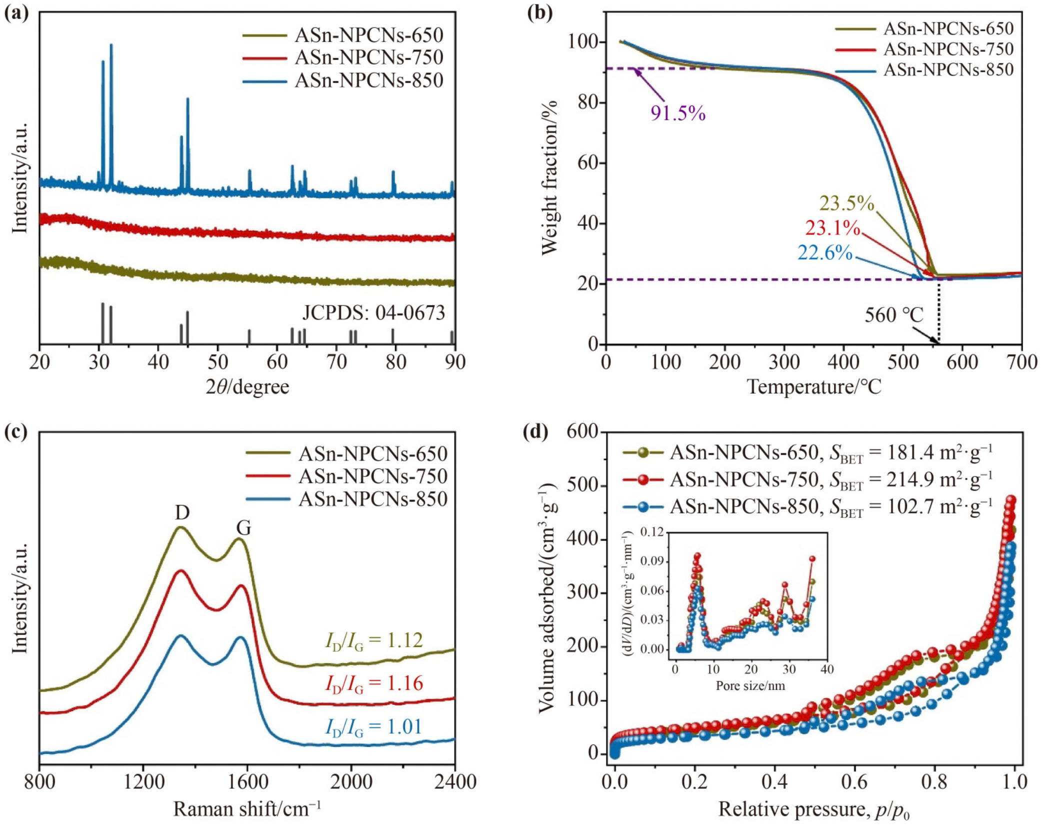

Fig. 3 Structural characterization: (**a**) XRD patterns of ASn-NPCNs-*T*; (**b**) TG curves of ASn-NPCNs-*T*; (**c**) Raman spectra of ASn-NPCNs-*T*; (**d**) N_2 adsorption/desorption isotherms and pore size distributions of ASn-NPCNs-*T*.

adsorbed water. The following reactions will happen along with the increased temperature:

$$C + O_2 \rightarrow CO_2 \tag{1}$$

$$Sn + O_2 \rightarrow SnO_2 \tag{2}$$

Hence, the contents of Sn are calculated to be 21.4% for ASn-NPCNs-650, 21.1% for ASn-NPCNs-750, and 20.3% for ASn-NPCNs-850 from the TG curves. This result shows that different temperatures do not affect the content of Sn in ASn-NPCNs-*T*. The structure characteristics of ASn-NPCNs-*T* samples are further investigated by Raman spectroscopy and N_2 adsorption/desorption isotherms. From the Raman spectra in Fig. 3(c), the value of the intensity ratio I_D/I_G in Raman spectra is used to verify structural defects in the carbon skeleton. Apparently, ASn-NPCNs-750 exhibits a higher I_D/I_G ratio of 1.16 than those of ASn-NPCNs-650 (1.12) and ASn-NPCNs-850 (1.01). The increase of carbon skeleton defects will provide more lithium-ion storage sites, which is conducive to the performance of LIBs [48]. In addition, the I_D/I_G ratio of ASn-NPCNs-750 is significantly higher than those of ASn-PC-750 (0.98) and NPCNs-750 (1.02), which may be due to the introduction of nitrogen and amorphous Sn, respectively (Fig. S4). The specific surface area and the pore size distribution of ASn-NPCNs-*T* are investigated via the N_2 adsorption/desorption isotherms (Fig. 3(d)). ASn-NPCNs-750 has a larger specific surface area ($214.9\ m^2\cdot g^{-1}$) than those of ASn-NPCNs-650 ($181.4\ m^2\cdot g^{-1}$) and ASn-NPCNs-850 ($102.7\ m^2\cdot g^{-1}$). Furthermore, ASn-NPCNs-750 owns a larger pore volume and a richer hierarchical pore distribution than those of ASn-NPCNs-650 and ASn-NPCNs-850. It is generally believed that mesopores promote the transfer of lithium ions and electrons, while micropores can supply rich active sites for the lithium-ion storage [49]. Consequently, based on the above advantages, ASn-NPCNs-750 may have the best lithium-ion storage performance.

In addition, XPS measurements are performed to evaluate elemental compositions of the ASn-NPCNs-*T* samples. The full spectra (Fig. 4(a)) indicate that the prepared ASn-NPCNs-*T* samples consist of C, N, O, and Sn elements, consistent with the element mapping results. The high-resolution C 1s spectrum of ASn-NPCNs-750

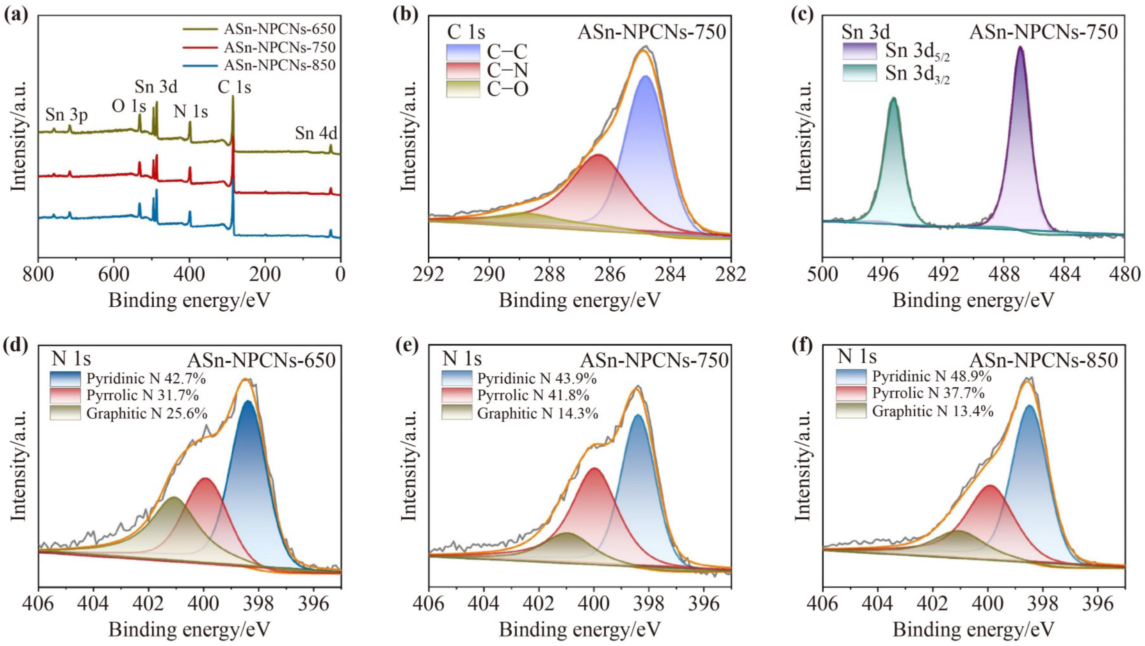

Fig. 4 Structural characterization: (**a**) XPS spectra of ASn-NPCNs-*T*; (**b**) C 1s high-resolution XPS spectra of ASn-NPCNs-750; (**c**) Sn 3d high-resolution XPS spectra of ASn-NPCNs-750; N 1s high-resolution XPS spectra of (**d**) ASn-NPCNs-650, (**e**) ASn-NPCNs-750, and (**f**) ASn-NPCNs-850.

can be divided into three peaks, including C−C (graphite carbon), C−N, and C−O located at 284.8, 286.4, and 288.9 eV, respectively (Fig. 4(b)) [50]. Figure 4(c) displays the high-resolution XPS spectrum of Sn 3d, there are two peaks located at 486.8 and 495.2 eV, which are assigned to Sn $3d_{5/2}$ and Sn $3d_{3/2}$, respectively [51]. Both ASn-NPCNs-650 and ASn-NPCNs-850 show similar high-resolution spectra of C 1s and Sn 3d to those of ASn-NPCNs-750 (Figs. S5 and S6). As illustrated in Figs. 4(d)–4(f), the high-resolution N 1s XPS spectra of ASn-NPCNs-*T* can be divided into three individual peaks at 398.4, 399.9, and 401.2 eV, assigning to pyridinic N, pyrrolic N, and graphitic N, respectively [52]. It is well known that the types of nitrogen have a tremendous impact on the structure and lithium-ion storage performance of the obtained carbon materials [49]. Edge-nitrogen dopants include pyridinic N and pyrrolic N, which are combined with two adjacent carbon atoms while leaving themselves at the edge of the defect or the carbon skeleton [53–54]. Moreover, the experimental and computational results illustrate that the defects in carbonaceous materials induced by edge nitrogen (pyridinic N and pyrrolic N) are key active sites for the lithium-ion storage, rather than graphitic N [55]. Table S1 depicts the quantitative analysis on three nitrogen doping types at different annealing temperatures. This result indicates that the three nitrogen doping types in ASn-NPCNs-*T* can be controlled by changing the annealing temperature. Interestingly, the edge-nitrogen content of ASn-NPCNs-*T* descends in the order: ASn-NPCNs-750 (14.01 at.%) > ASn-NPCNs-850 (13.14 at.%) > ASn-NPCNs-650 (13.01 at.%). A similar phenomenon has been confirmed in previously reported literature [49,53]. According to above results, it can be inferred that ASn-NPCNs-750 may have better lithium-ion storage performance than that of ASn-NPCNs-650 and ASn-NPCNs-850.

The lithium-ion storage performance of ASn-NPCNs-*T* electrodes was evaluated by assembling CR2032-type coin half-cells. Figure 5(a) illustrates the first three CV curves of the ASn-NPCNs-750 electrode between 0.01 and 3.0 V at a scan rate of 0.1 mV·s^{-1}. The large reduction peak appears at about 0.74 V during the first cathodic scan but disappears in the following cycles, regarded as the formation of solid-electrolyte interface (SEI) films [56]. The cascade of the reduction peak below 0.5 V is attributed to the Li_xSn alloying process and the lithium-ion insertion into ASn-NPCNs-750 [35]. In the anodic scan, the oxidation peak at 0.30 V demonstrates the extraction of lithium ions from ASn-NPCNs-750, while the oxidation peak at 0.65 V is regarded as the dealloying process of Li_xSn [35]. As illustrated in Fig. S7,

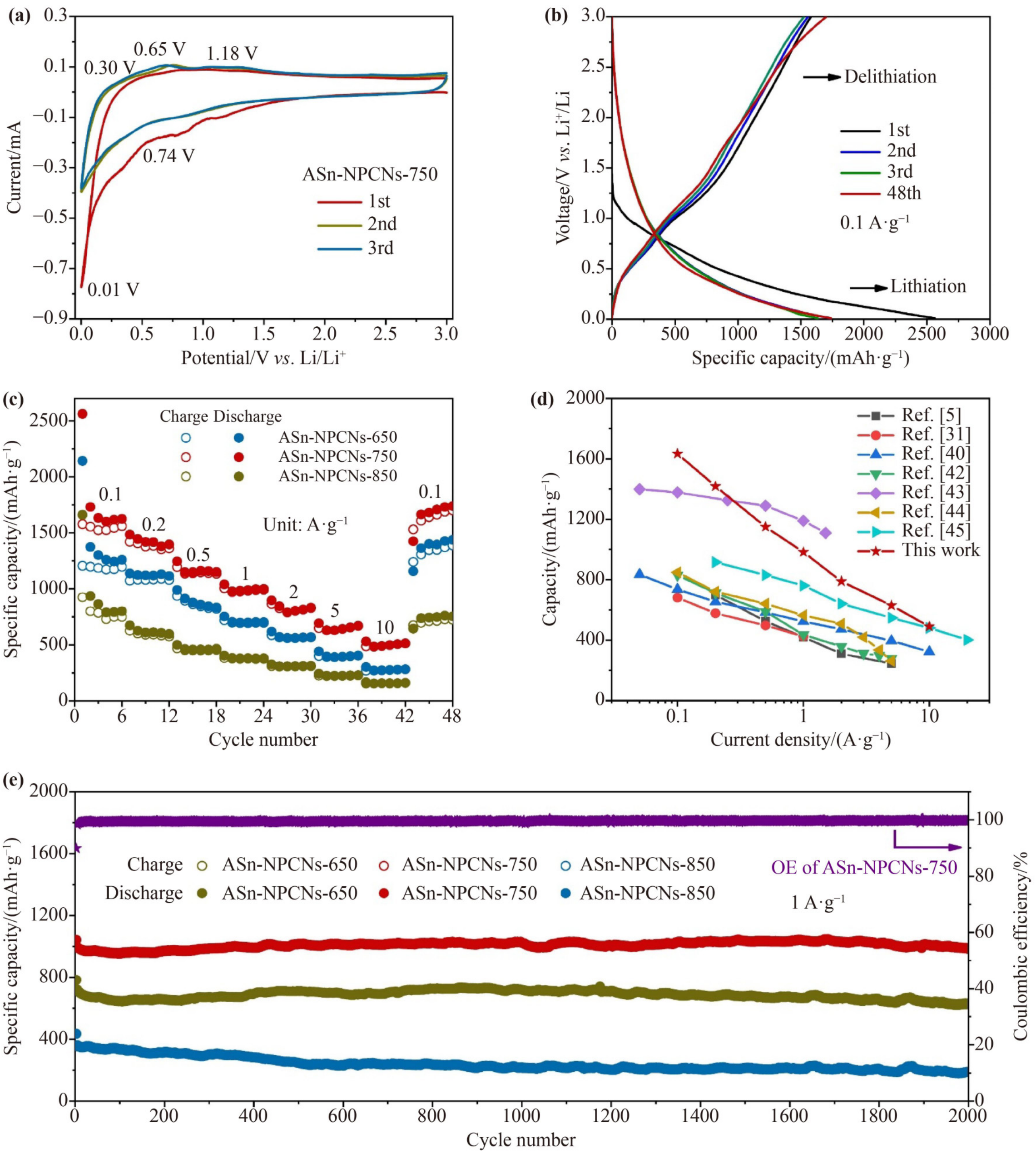

Fig. 5 Electrochemical performances of ASn-NPCNs-*T* in LIBs: (**a**) CV curves at 0.1 mV·s^{-1} and (**b**) discharge/charge profiles of ASn-NPCNs-750. (**c**) Rate performance of ASn-NPCNs-*T* half-cells at 25 °C in the voltage range of 0–3 V. (**d**) Comparison of the rate performance of ASn-NPCNs-750 with reported Sn/C materials for LIBs. (**e**) Long-term cycling stability of ASn-NPCNs-750 at 1 A·g^{-1} for 2000 cycles.

the CV curves of ASn-NPCNs-650 and ASn-NPCNs-850 also exhibit similar characteristics. In addition, the curve of the 3rd scan overlaps well with that of the 2nd one, indicating superior electrochemical reversibility of the ASn-NPCNs-750 electrode.

The galvanostatic discharge/charge tests of ASn-NPCNs-*T* electrodes were carried out between 0.01 and 3.0 V to evaluate their lithium-storage capabilities. The typical galvanostatic discharge/charge curves of the 1st, 2nd, 3rd, and 48th cycles of ASn-NPCNs-750 are displayed in Fig. 5(b). The initial lithiation and delithiation specific capacities are 2563 and 1578 mAh·g^{-1}, respectively. The initial irreversible capacity may be due to the formation of the SEI film, the irreversible lithium storage in carbon materials, and the conversion reaction of Sn. The lithiation/delithiation specific capacity decreases in the 2nd and 3rd cycles and then increases in the 48th cycle, indicating that there is an activation process in the initial several cycles. The rate capacities of ASn-NPCNs-*T* electrodes at the current density from 0.1 to 10 $\mathrm{A{\cdot}g^{-1}}$ are depicted in Fig. 5(c). Specifically, the ASn-NPCNs-750 electrode delivers highly reversible capacities of 1643, 1419, 1150, 983, 789, 630, and 490 $\mathrm{mAh{\cdot}g^{-1}}$ at 0.1, 0.2, 0.5, 1, 2, 5, and 10 $\mathrm{A{\cdot}g^{-1}}$, respectively. After the current density is shifted to 0.1 $\mathrm{A{\cdot}g^{-1}}$, a higher capacity of 1681 $\mathrm{mAh{\cdot}g^{-1}}$ can be retained, confirming its excellent reversibility. The discharge/charge curves of the ASn-NPCNs-750 electrode at the current density from 0.1 to 10 $\mathrm{A{\cdot}g^{-1}}$ are illustrated in Fig. S8. As for the sample ASn-NPCNs-650, lower rate performance is mainly owing to the lower edge-nitrogen doping level in the carbon substrate [53], while the poor rate performance for ASn-NPCNs-850 is due to the presence of crystalline Sn. In addition, both ASn-PC-750 and NPCNs-750 show poorer rate performance than that of ASn-NPCNs-750 (Fig. S9). By contrast, the superior rate performance of ASn-NPCNs-750 outperforms many recently reported Sn/C anodes for LIBs (Fig. 5(d)) [57–63]. To further understand the properties of those materials, the long-term cycling performance of ASn-NPCNs-*T* electrodes was measured at the current density of 1 $\mathrm{A{\cdot}g^{-1}}$. As illustrated in Fig. 5(e), ASn-NPCNs-750 remains a high capacity of 988 $\mathrm{mAh{\cdot}g^{-1}}$ after 2000 cycles at the current density of 1 $\mathrm{A{\cdot}g^{-1}}$, with a capacity retention of 98.9%, which is better than those of ASn-NPCNs-650 and ASn-NPCNs-850. Table S2 illustrates that the cycling performance of ASn-NPCNs-750 is better than many reported Sn/C anode materials for LIBs. The excellent long-term cycling stability of the ASn-NPCNs-750 electrode can be attributed to amorphous Sn that can adapt to the mechanical stress in the lithiation/delithiation process [22,58]. According to above results, it is deduced that the impressive lithium-ion storage performance of ASn-NPCNs-750 derives from the synergistic effect of amorphous Sn and high edge-nitrogen-doped level porous carbon nanosheets that provide it with multiple advantages containing abundant defect sites, high specific surface area, and rich hierarchical pores for the lithium-ion storage.

To reveal the excellent lithium-ion storage dynamics and the mechanism of ASn-NPCNs-*T* electrodes, CV measurements were taken at 0.3–1.3 $\mathrm{mV{\cdot}s^{-1}}$ (Figs. 6(a)–6(c)). It can be noted that with the increase of the scan rate, the existing depolarization peak expands to a higher potential range, indicating that the lithium-ion storage process of the capacitive behavior is dominant [49]. The capacitive mechanism can be explored by following equations:

$$i = av^b \tag{3}$$

$$\lg i = b \lg v + \lg a \tag{4}$$

where a and b are variable positive numbers, v is the scan rate, and i is the peak current. It is generally believed that the value of b can be determined by plotting the lg i–lg v curve [64]. When the b value is close to 0.5, the electrochemical reaction is dominated by the diffusion-controlled process, while close to 1.0 means that the lithium-ion storage is predominantly contributed by the capacitive-controlled process. As illustrated in Fig. S10, all b values of ASn-NPCNs-*T* electrodes are between 0.5 and 1.0, indicating that the lithium-ion storage mechanism is the hybrid process containing the diffusion-controlled and the capacitive-controlled processes. Furthermore, the capacitive-controlled contribution of the lithium-ion storage to the total capacity can be estimated by the following equation:

$$i(v) = k_1 v + k_2 v^{1/2} \tag{5}$$

where, k_1 and k_2 are constants by linear fitting, and $k_1 v$ and $k_2 v^{1/2}$ represent the capacitive-controlled contribution and the diffusion-controlled contribution, respectively. Figures 6(d)–6(f) reveal the capacitive-controlled contribution ratios of ASn-NPCNs-*T* electrodes at the scan rate of 1 $\mathrm{mV{\cdot}s^{-1}}$. Calculated by integral fitting, ASn-NPCNs-750 exhibits a capacitive-controlled contribution of 83.4%, which is higher than those of ASn-NPCNs-650 (78.5%) and ASn-NPCNs-850 (67.8%). As shown in Fig. 6(g), the capacitive-controlled contributions of ASn-NPCNs-*T* electrodes are improved as the scan rate increases. Apparently, the ASn-NPCNs-750 electrode always maintains an absolute advantage in the capacitive-controlled contribution. The enhanced capacitive-controlled contribution is due to that the amorphous Sn and high edge-nitrogen-doped level introduce more surface defects, and the rich hierarchical pores nanosheet structure increases the specific surface area, thus facilitating the rapid capacitive mechanism of the ASn-NPCNs-750 electrode. These results illustrate that the ASn-NPCNs-750 electrode with high capacitive-controlled contribution is more favorable to the high-rate performance.

Moreover, the EIS measurement was further performed

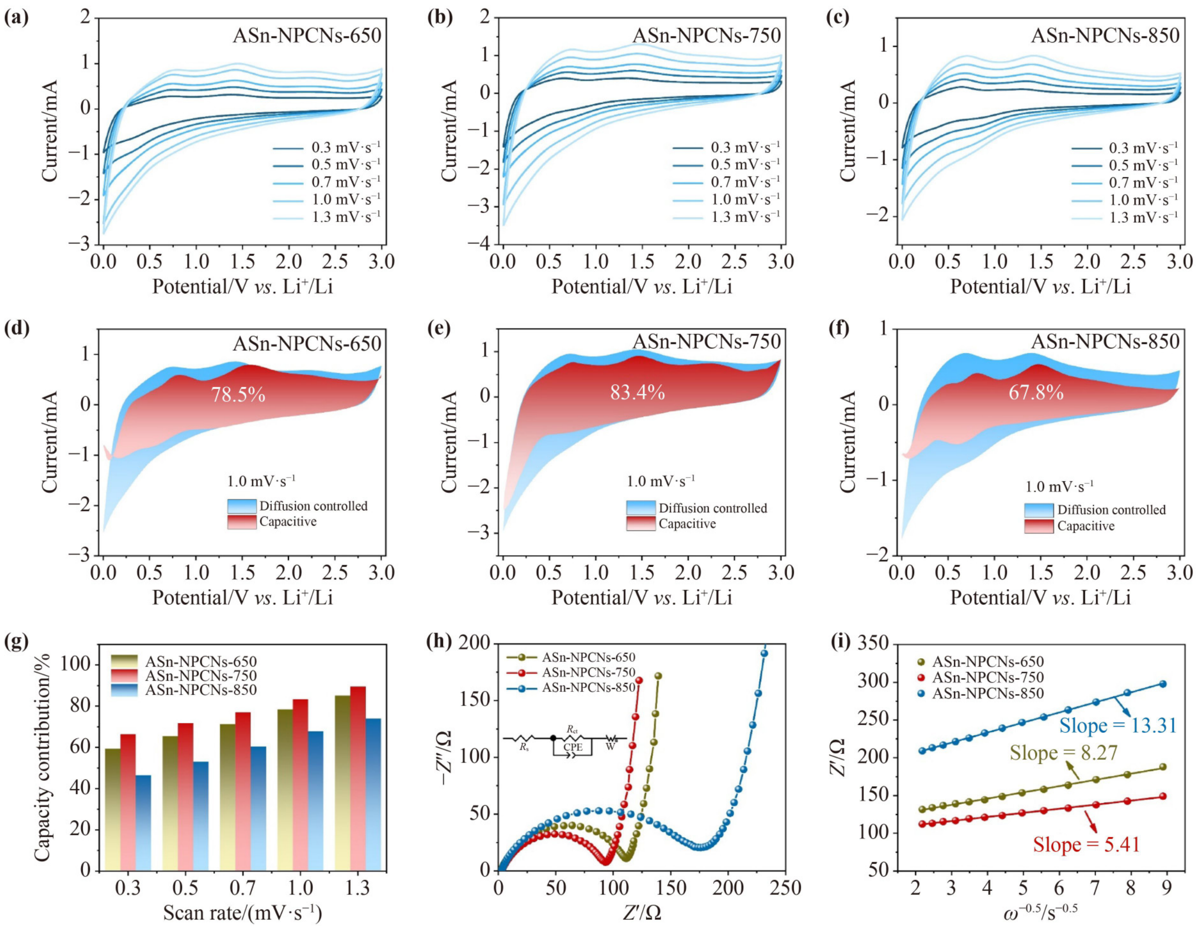

Fig. 6 Quantitative analysis of the lithium-ion storage mechanism: CV curves of (**a**) ASn-NPCNs-650, (**b**) ASn-NPCNs-750, and (**c**) ASn-NPCNs-850 at different scan rates of 0.3–1.3 mV·s^{-1}; capacitive-controlled contribution in (**d**) ASn-NPCNs-650, (**e**) ASn-NPCNs-750, and (**f**) ASn-NPCNs-850 at a scan rate of 1.0 mV·s^{-1}; (**g**) contribution ratios of the capacitive process for ASn-NPCNs-*T* at different scan rates; (**h**) Nyquist plots for ASn-NPCNs-*T*; (**i**) the liner relation of Z' versus $\omega^{-0.5}$ for ASn-NPCNs-*T*.

to recognize the rapid electrochemical reaction kinetics of ASn-NPCNs-*T* electrodes. As demonstrated in Fig. 6(h), the Nyquist plots of ASn-NPCNs-*T* electrodes exhibit the same outline with a semicircle (R_{ct} representing the charge transfer resistance) and an oblique line (W representing the Warburg diffusion resistance that indicates the lithium-ion diffusion process inside the electrode). The R_s (resistance of the electrolyte and other inherent resistances) can be acquired from the intercept of the semicircle on the *x*-axis in the high-frequency region. The corresponding values of R_{ct} and R_s are summarized in Table S3, which are obtained by the equivalent electrical circuit in Fig. 6(h). It can be found that the ASn-NPCNs-750 electrode has a smaller R_{ct} (93.4 Ω) than those of the ASn-NPCNs-650 electrode (112.3 Ω) and the ASn-NPCNs-850 electrode (177.8 Ω), demonstrating its better kinetics among ASn-NPCNs-*T* electrodes. Similarly, the slope of the straight line is inversely proportional to W (defined as the Warburg diffusion resistance), in which the W value of ASn-NPCNs-750 is the smallest. Figure 6(i) illustrates the fitting curves between Z' and $\omega^{-0.5}$, in which the slope of the fitting curve is inversely proportional to the lithium-ion diffusion rate [49]. The ASn-NPCNs-750 electrode maintains the minimum slope of the fitting curve, revealing the maximum lithium-ion transfer rate among ASn-NPCNs-*T* electrodes. Furthermore, the lithium-ion diffusion coefficient (D_{Li^+}) values in ASn-NPCNs-*T* electrodes are investigated from following equations [65]:

$$D_{\mathrm{Li}^+} = \frac{R^2 T_a^2}{2A^2 n^4 F^4 C^2 \sigma^2} \tag{6}$$

$$Z' = R_s + R_{ct} + \sigma\omega^{-1/2} \tag{7}$$

where R is the gas constant, T_a is the absolute temperature, A is the surface area of the electrode, n is the number of transfer electrons per mole of the active material involved in the electrode reaction, F is the Faraday constant, C is the molar concentration of lithium ion, Z' is the real part of the impedance, and σ is the Warburg factor associated with Z'. As demonstrated in Table S3, the ASn-NPCNs-750 electrode shows a higher D_{Li^+} (2.42×10^{-12} $\mathrm{cm^2 \cdot s^{-1}}$) than those of the ASn-NPCNs-650 electrode (7.64×10^{-13} $\mathrm{cm^2 \cdot s^{-1}}$) and the ASn-NPCNs-850 electrode (6.41×10^{-14} $\mathrm{cm^2 \cdot s^{-1}}$), leading to a faster lithium-ion transport. This result implies that the D_{Li^+} value of the ASn-NPCNs-750 electrode is improved remarkably, ascribing to the high edge-nitrogen-doped level that enhances the electronic conductivity and the lithium-ion transfer rate, thus improving the fast-charging performance.

4 Conclusions

Novel ASn-NPCNs are successfully acquired through a hydrothermal and annealing strategy, which delivers enhanced lithium-ion storage performance. The synergistic effect of amorphous Sn and the high edge-nitrogen-doped level introduce more surface defects, and the rich hierarchical pores nanosheet structure increases the specific surface area, thereby facilitating the rapid electrochemical reaction kinetics of the ASn-NPCNs-750 electrode. Consequently, the ASn-NPCNs-750 electrode shows high capacity ($1643\ \mathrm{mAh \cdot g^{-1}}$ at $0.1\ \mathrm{A \cdot g^{-1}}$), remarkable rate performance ($490\ \mathrm{mAh \cdot g^{-1}}$ at $10\ \mathrm{A \cdot g^{-1}}$), and superior cycling stability ($988\ \mathrm{mAh \cdot g^{-1}}$ at $1\ \mathrm{A \cdot g^{-1}}$ after 2000 cycles with a capacity retention of 98.9%). Furthermore, the enhanced lithium-ion storage of the ASn-NPCNs-750 electrode is ascribed to the rapid capacitive mechanism which is demonstrated by the in-depth electrochemical kinetic analysis. This work provides an attainable strategy for developing Sn/C LIBs anode materials and supplies a reference for adjusting the capacitive mechanism to accomplish enhanced lithium-ion storage.

Disclosure of potential conflicts of interests The authors declare no conflict of interest.

Acknowledgements We gratefully acknowledge the financial supports from the National Natural Science Foundation of China (Grant Nos. 22238012, 22178384, and 21908245), and the Science Foundation of China University of Petroleum, Beijing (Grant No. ZX20220079).

Electronic supplementary information Supplementary materials can be found in the online version at https://doi.org/10.1007/s11706-023-0651-y, which include Figs. S1–S10 and Tables S1–S3.

References

[1] Xiao J, Li Q, Bi Y, et al. Understanding and applying coulombic efficiency in lithium metal batteries. Nature Energy, 2020, 5(8): 561–568

[2] Chae S, Ko M, Kim K, et al. Confronting issues of the practical implementation of Si Anode in high-energy lithium-ion batteries. Joule, 2017, 1(1): 47–60

[3] Zhou J, Jiang Z, Niu S, et al. Self-standing hierarchical P/CNTs@rGO with unprecedented capacity and stability for lithium and sodium storage. Chem, 2018, 4(2): 372–385

[4] Liang L, Sun X, Zhang J, et al. *In situ* synthesis of hierarchical core double-shell Ti-doped $\mathrm{LiMnPO_4@NaTi_2(PO_4)_3@C/3D}$ graphene cathode with high-rate capability and long cycle life for lithium-ion batteries. Advanced Energy Materials, 2019, 9: 1–15

[5] Xu Z, Zeng Y, Wang L, et al. Nanoconfined phosphorus film coating on interconnected carbon nanotubes as ultrastable anodes for lithium ion batteries. Journal of Power Sources, 2017, 356: 18–26

[6] Xia Y, Han S, Zhu Y, et al. Stable cycling of mesoporous $\mathrm{Sn_4P_3/SnO_2@C}$ nanosphere anode with high initial coulombic efficiency for Li-ion batteries. Energy Storage Materials, 2019, 18: 125–132

[7] Subramaniyam C, Tai Z, Mahmood N, et al. Unlocking the potential of amorphous red phosphorus films as a long-term stable negative electrode for lithium batteries. Journal of Materials Chemistry A: Materials for Energy and Sustainability, 2017, 5(5): 1925–1929

[8] Zhang X, Cheng X, Zhang Q. Nanostructured energy materials for electrochemical energy conversion and storage: a review. Journal of Energy Chemistry, 2016, 25(6): 967–984

[9] Zhou X, Liu Q, Jiang C, et al. Strategies towards low-cost dual-ion batteries with high performance. Angewandte Chemie International Edition, 2020, 59(10): 3802–3832

[10] Sun Y, Liu N, Cui Y. Promises and challenges of nanomaterials for lithium-based rechargeable batteries. Nature Energy, 2016, 1: 16071

[11] Deng J, Yu X, Qin X, et al. Carbon sphere-templated synthesis of porous yolk–shell $\mathrm{ZnCo_2O_4}$ spheres for high-performance lithium storage. Journal of Alloys and Compounds, 2019, 780: 65–71

[12] Niu F, Shao Z, Gao H, et al. Si-doped graphene nanosheets for NO_x gas sensing. Sensors and Actuators B: Chemical, 2021, 328: 129005

[13] Li X, Chen G, Le Z, et al. Well-dispersed phosphorus nanocrystals within carbon via high-energy mechanical milling for high performance lithium storage. Nano Energy, 2019, 59: 464–471

[14] Sun Y, Wang L, Li Y, et al. Design of red phosphorus nanostructured electrode for fast-charging lithium-ion batteries with high energy density. JOULE, 2019, 3(4): 1080–1093

[15] Wang Y, Tian L, Yao Z, et al. Enhanced reversibility of red phosphorus/active carbon composite as anode for lithium ion batteries. Electrochimica Acta, 2015, 163: 71–76

[16] Huang B, Pan Z, Su X, et al. Tin-based materials as versatile anodes for alkali (earth)-ion batteries. Journal of Power Sources, 2018, 395: 41–59

[17] Shin J H, Song J Y. Electrochemical properties of Sn-decorated SnO nanobranches as an anode of Li-ion battery. Nano Convergence, 2016, 3(1): 9

[18] Wang J, Li W, Wang F, et al. Controllable synthesis of SnO_2@C yolk–shell nanospheres as a high-performance anode material for lithium ion batteries. Nanoscale, 2014, 6(6): 3217–3222

[19] Yang L, Dai T, Wang Y, et al. Chestnut-like SnO_2/C nanocomposites with enhanced lithium ion storage properties. Nano Energy, 2016, 30: 885–891

[20] Park J W, Park C M. Electrochemical Li topotactic reaction in layered SnP_3 for superior Li-ion batteries. Scientific Reports, 2016, 6(1): 35980

[21] Miao C, Liu M, He Y, et al. Monodispersed SnO_2 nanospheres embedded in framework of graphene and porous carbon as anode for lithium ion batteries. Energy Storage Materials, 2016, 3: 98–105

[22] Zhang B, Huang J, Kim J. Ultrafine amorphous SnO_x embedded in carbon nanofiber/carbon nanotube composites for Li-ion and Na-ion batteries. Advanced Functional Materials, 2015, 25(32): 5222–5228

[23] Yi Z, Tian X, Han Q, et al. Synthesis of polygonal Co_3Sn_2 nanostructure with enhanced magnetic properties. RSC Advances, 2016, 6(46): 39818–39822

[24] Kim M G, Sim S, Cho J. Novel core–shell Sn–Cu anodes for lithium rechargeable batteries prepared by a redox-transmetalation reaction. Advanced Materials, 2010, 22(45): 5154–5158

[25] Yi Z, Tian X, Han Q, et al. One-step synthesis of Ni_3Sn_2@reduced graphene oxide composite with enhanced electrochemical lithium storage properties. Electrochimica Acta, 2016, 192: 188–195

[26] Ding Y L, Wen Y, van Aken P A, et al. Large-scale low temperature fabrication of SnO_2 hollow/nanoporous nanostructures: the template-engaged replacement reaction mechanism and high-rate lithium storage. Nanoscale, 2014, 6(19): 11411–11418

[27] Xu L, Kim C, Shukla A K, et al. Monodisperse Sn nanocrystals as a platform for the study of mechanical damage during electrochemical reactions with Li. Nano Letters, 2013, 13(4): 1800–1805

[28] Zhu C, Xia X, Liu J, et al. TiO_2 nanotube@SnO_2 nanoflake core–branch arrays for lithium-ion battery anode. Nano Energy, 2014, 4: 105–112

[29] Duan Y, Du S, Tao H, et al. Sn@C composite for lithium ion batteries: amorphous vs. crystalline structures. Ionics, 2021, 27(4): 1403–1412

[30] Xu Y, Liu Q, Zhu Y, et al. Uniform nano-Sn/C composite anodes for lithium ion batteries. Nano Letters, 2013, 13(2): 470–474

[31] Nam D, Kim J, Lee J, et al. Tunable Sn structures in porosity-controlled carbon nanofibers for all-solid-state lithium-ion battery anodes. Journal of Materials Chemistry A: Materials for Energy and Sustainability, 2015, 3(20): 11021–11030

[32] Sun L, Wang X, Susantyoko R, et al. High performance binder-free Sn coated carbon nanotube array anode. Carbon, 2015, 82: 282–287

[33] Luo B, Qiu T, Ye D, et al. Tin nanoparticles encapsulated in graphene backboned carbonaceous foams as high-performance anodes for lithium-ion and sodium-ion storage. Nano Energy, 2016, 22: 232–240

[34] Ma G, Yang W, Xu C, et al. Nitrogen-doped porous carbon embedded Sn/SnO nanoparticles as high-performance lithium-ion battery anode. Electrochimica Acta, 2022, 428: 140898

[35] Zhu Z, Wang S, Du J, et al. Ultrasmall Sn nanoparticles embedded in nitrogen-doped porous carbon as high-performance anode for lithium-ion batteries. Nano Letters, 2014, 14(1): 153–157

[36] Kang S, Li X, Yin C, et al. Three-dimensional mesoporous sandwich-like g-C_3N_4-interconnected $CuCo_2O_4$ nanowires arrays as ultrastable anode for fast lithium storage. Journal of Colloid and Interface Science, 2019, 554: 269–277

[37] Zuo Y, Xu X, Zhang C, et al. SnS_2/g-C_3N_4/graphite nanocomposites as durable lithium-ion battery anode with high pseudocapacitance contribution. Electrochimica Acta, 2020, 349: 136369

[38] Adekoya D, Li M, Hankel M, et al. Design of a 1D/2D C_3N_4/rGO composite as an anode material for stable and effective potassium storage. Energy Storage Materials, 2020, 25: 495–501

[39] Zou W, Deng B, Hu X, et al. Crystal-plane-dependent metal oxide-support interaction in CeO_2/g-C_3N_4 for photocatalytic hydrogen evolution. Applied Catalysis B: Environmental, 2018, 238: 111–118

[40] Jin H, Liu X, Jiao Y, et al. Constructing tunable dual active sites on two-dimensional C_3N_4@MoN hybrid for electrocatalytic hydrogen evolution. Nano Energy, 2018, 53: 690–697

[41] Kennedy R, Marr K, Ezekoye O. Gas release rates and properties from lithium cobalt oxide lithium ion battery arrays. Journal of Power Sources, 2021, 487: 229388

[42] Zeng G, Deng Y, Yu X, et al. Ultrathin g-C_3N_4 as a hole extraction layer to boost sunlight-driven water oxidation of $BiVO_4$-based photoanode. Journal of Power Sources, 2021, 494: 229701

[43] Zhao W, Wang J, Yin R, et al. Single-atom Pt supported on holey ultrathin g-C_3N_4 nanosheets as efficient catalyst for Li-O_2 batteries. Journal of Colloid and Interface Science, 2020, 564: 28–36

[44] Vinoth S, Subramani K, Ong W J, et al. CoS_2 engulfed ultra-thin S-doped g-C_3N_4 and its enhanced electrochemical performance in hybrid asymmetric supercapacitor. Journal of Colloid and Interface Science, 2021, 584: 204–215

[45] Wang S, Shi Y, Fan C, et al. Layered g-C_3N_4@reduced graphene oxide composites as anodes with improved rate performance for lithium-ion batteries. ACS Applied Materials & Interfaces, 2018, 10(36): 30330–30336

[46] Hou Y, Li J, Wen Z, et al. N-doped graphene/porous g-C_3N_4 nanosheets supported layered-MoS_2 hybrid as robust anode materials for lithium-ion batteries. Nano Energy, 2014, 8: 157–164

[47] Zhang B, Yu Y, Huang Z, et al. Exceptional electrochemical performance of freestanding electrospun carbon nanofiber anodes containing ultrafine SnO_x particles. Energy & Environmental Science, 2012, 5(12): 9895–9902

[48] Hu H, Li Q, Li L, et al. Laser irradiation of electrode materials for energy storage and conversion. Matter, 2020, 3(1): 95–126

[49] Xu C, Yang W, Ma G, et al. Edge-nitrogen enriched porous carbon nanosheets anodes with enlarged interlayer distance for fast charging sodium-ion batteries. Small, 2022, 18(48): 2204375

[50] Li Y, Yang W, Tu Z, et al. Water-soluble salt-templated strategy to regulate mesoporous nanosheets-on-network structure with active mixed-phase CoO/Co_3O_4 nanosheets on graphene for superior lithium storage. Journal of Alloys and Compounds, 2021, 857: 157626

[51] Qin J, He C, Zhao N, et al. Graphene networks anchored with sn@graphene as lithium ion battery anode. ACS Nano, 2014, 8(2): 1728–1738

[52] Yang T, Zhong J, Liu J, et al. A general strategy for antimony-based alloy nanocomposite embedded in Swiss-cheese-like nitrogen-doped porous carbon for energy storage. Advanced Functional Materials, 2021, 31(13): 2009433

[53] Liu J, Zhang Y, Zhang L, et al. Graphitic carbon nitride (g-C_3N_4)-derived N-rich graphene with tuneable interlayer distance as a high-rate anode for sodium-ion batteries. Advanced Materials, 2019, 31(24): 1901261

[54] Zhang W, Yin J, Sun M, et al. Direct pyrolysis of supermolecules: an ultrahigh edge-nitrogen doping strategy of carbon anodes for potassium-ion batteries. Advanced Materials, 2020, 32(25): 2000732

[55] Qin D, Wang L, Zeng X, et al. Tailored edge-heteroatom tri-doping strategy of turbostratic carbon anodes for high-rate performance lithium and sodium-ion batteries. Energy Storage Materials, 2023, 54: 498–507

[56] Tian W, Zhang H, Duan X, et al. Porous carbons: structure-oriented design and versatile applications. Advanced Functional Materials, 2020, 30(17): 1909265

[57] Youn D H, Heller A, Mullins C B. Simple synthesis of nanostructured Sn/nitrogen-doped carbon composite using nitrilotriacetic acid as lithium ion battery anode. Chemistry of Materials, 2016, 28(5): 1343–1347

[58] Cheng Y, Yi Z, Wang C, et al. Controllable fabrication of C/Sn and C/SnO/Sn composites as anode materials for high-performance lithium-ion batteries. Chemical Engineering Journal, 2017, 330: 1035–1043

[59] Ying H, Zhang S, Meng Z, et al. Ultrasmall Sn nanodots embedded inside N-doped carbon microcages as high-performance lithium and sodium ion battery anodes. Journal of Materials Chemistry A: Materials for Energy and Sustainability, 2017, 5(18): 8334–8342

[60] Chang X, Wang T, Liu Z, et al. Ultrafine Sn nanocrystals in a hierarchically porous N-doped carbon for lithium ion batteries. Nano Research, 2017, 10(6): 1950–1958

[61] Park M G, Lee D H, Jung H, et al. Sn-based nanocomposite for Li-ion battery anode with high energy density, rate capability, and reversibility. ACS Nano, 2018, 12(3): 2955–2967

[62] Liu X, Li X, Yu J, et al. Ultrasmall Sn nanoparticles embedded in N-doped carbon nanospheres as long cycle life anode for lithium ion batteries. Materials Letters, 2018, 223: 203–206

[63] Mo R, Tan X, Li F, et al. Tin-graphene tubes as anodes for lithium-ion batteries with high volumetric and gravimetric energy densities. Nature Communications, 2020, 11(1): 1374

[64] Xu C, Ma G, Yang W, et al. One-step reconstruction of acid treated spent graphite for high capacity and fast charging lithium-ion batteries. Electrochimica Acta, 2022, 415: 140198

[65] Zhu L, Wang Y, Wang M, et al. High edge-nitrogen-doped porous carbon nanosheets with rapid pseudocapacitive mechanism for boosted potassium-ion storage. Carbon, 2022, 187: 302–309